01 Jul 2020

A Design Of Taper-Like Etched Multicore Fiber Refractive Index-Insensitive A Temperature Highly Sensitive Mach-Zehnder Interferometer

Farhan Mumtaz
Missouri University of Science and Technology, mfmawan@mst.edu

Pu Cheng

Chi Li

Shu Cheng

et. al. For a complete list of authors, see https://scholarsmine.mst.edu/ele_comeng_facwork/5072

Recommended Citation

F. Mumtaz et al., "A Design Of Taper-Like Etched Multicore Fiber Refractive Index-Insensitive A Temperature Highly Sensitive Mach-Zehnder Interferometer," *IEEE Sensors Journal*, vol. 20, no. 13, pp. 7074 - 7081, article no. 9025181, Institute of Electrical and Electronics Engineers, Jul 2020.
The definitive version is available at https://doi.org/10.1109/JSEN.2020.2978533

A Design of Taper-Like Etched Multicore Fiber Refractive Index-Insensitive a Temperature Highly Sensitive Mach-Zehnder Interferometer

Farhan Mumtaz, Pu Cheng, Chi Li, Shu Cheng, Cheng Du, Minghong Yang, Yutang Dai, and Wenbin Hu

***Abstract*—We propose and demonstrate Mach-Zehnder interferometer (MZI), which is the refractive index (RI) insensitive and temperature highly sensitive based on etched multicore fiber (MCF) structure. The MCF and Fiber Bragg Grating (FBG) are used as hybrid sensing elements. The fabrication of the interferometer is provided a new taper-like structure by etching the MCF to further expose the side cores to the surroundings. The interferometer has produced a sensitivity of 103.2pm/°C within the ambient temperature up-to 70°C. Moreover, the superior temperature sensitivity is 89.19pm/°C, 66.64pm/°C, 56.42pm/°C in the range of 24°C to 130°C, and RI-insensitive in the range of 1.34 to 1.38, for different waists of etched seven-core fiber interferometers (E7CFIs) ~ 84.70μm, 93.10μm, 108.67μm, respectively. Compared with the conventional FBGs, the sensitivity of the interferometer is significantly improved by 8 times. E7CFI's novel and advantageous features can easily be distinguished other devices. Besides, the proposed sensing architecture is compact, easy to fabricate, highly sensitive, easy to reproduce, and makes it an inexpensive fiber optic device.**

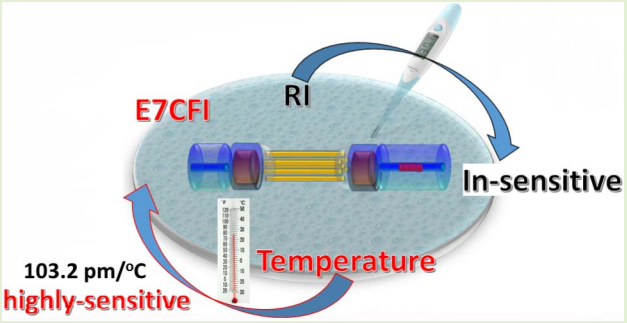

***Index Terms*—Mach-Zehnder interferometer, multicore fiber, etching technique.**

I. Introduction

IN THE field of fiber optic sensing, a wide range of probing and their applications have been presented such as strain [1], temperature [2], refractive index [3], humidity [4], curvature [5], liquid level [6] and pressure [7]. Among them, few have been realized by the multi-mode coupling techniques. The phenomenon of multimode coupling leads to multimode interference (MMI), which has a significant contribution to the sensing mechanism. The sensing mechanism has involved multiple input parameters to sense such as temperature, strain, RI, etc. Although, MMI-based optical sensors have been extensively discussed in the literatures [8]–[14]. These sensors can be fabricated by splicing a section of multimode fiber between two single-mode fibers (SMF), so-called SMS sensors. In the collection of multi-core coupled optical fibers, MCF has become a hot topic today because of its easy implementation using in-line coupling technique. Few optical sensors based on multi-core fiber have been proposed to demonstrate temperature and RI sensing using tapering and etching procedures [15]–[21]. On the other hand, being a predominant optical temperature sensor, the fiber Bragg grating (FBG) is the one who has relatively simple, reliable and compatible characteristics in many practical applications, although its sensitivity response is relatively low compared with the optical interferometers.

The low loss etching is a unique technique to assemble different optical fiber waists. While the fast etching technique shows a shorter etching time but results demonstrated higher transmission loss. The Zhang [22] and Lee [23] have been proposed a slower etching methodology, which could help

Manuscript received February 12, 2020; accepted March 2, 2020. Date of publication March 5, 2020; date of current version June 4, 2020. This work was supported in part by the Major Technique Innovation Program of Hubei Province of China under Grant 2018AAA016, and in part by the National Natural Science Foundation of China under Grant 51975442. The associate editor coordinating the review of this article and approving it for publication was Dr. Qiang Wu. *(Corresponding authors: Yutang Dai; Wenbin Hu.)*

Farhan Mumtaz is with the National Engineering Laboratory for Fiber Optic Sensing Technology, Wuhan University of Technology, Wuhan 430070, China, and also with the School of Information and Communication Engineering, Wuhan University of Technology, Wuhan 430070, China.

Pu Cheng, Chi Li, Shu Cheng, Minghong Yang, Yutang Dai, and Wenbin Hu are with the National Engineering Laboratory for Fiber Optic Sensing Technology, Wuhan University of Technology, Wuhan 430070, China (e-mail: daiyt6688@whut.edu.cn; wenbinhu_whut@163.com).

Cheng Du is with FiberHome Telecommunication Technologies Company Ltd., Wuhan 430205, China.

Digital Object Identifier 10.1109/JSEN.2020.2978533

to obtain a smooth waist surface and better control over the final waist diameter. However, the non-linearity was observed during the etching process, which could be caused by the faster evaporation of hydrofluoric acid (HF) in the surrounding medium than deionized water. Therefore, the contribution of slower etching techniques has a significant impact on obtaining the desired smooth waist diameter of the optical fibers.

The fiber optic sensors based on the MZI principle have been studied for temperature specifically and other applied parameter sensing [24]–[28]. From ambient to high-temperature sensing, a variety of temperature sensing interferometers based on SMFs and specially designed optical fibers have been discussed [29]–[32]. These literatures have been reported analogy MZI structures with the maximum temperature sensitivity of 54.57pm/°C [3], 59.02pm/°C [29], 55.81pm/°C [33] and 82pm/°C [18] respectively. However, for these MZI interferometers, apart from FBG, they rarely have functions that could be temperature sensitive and RI insensitive. Compared with the category of interferometers, the FBGs have offered a temperature sensitivity of 10pm/°C, which is relatively low. The E7CFIs have compact design with higher sensitive responses that could easily be maintained to a level that can distinguish the reported interferometers [34], [35]. Therefore, the classification of MZI-based sensors insensitive to RI but highly sensitive to temperature, which is a convincing argument for researchers.

In this paper, we are experimentally demonstrated MZI coupled etched multicore fiber (EMCF), which is further used to fabricate the SMF-MMF-EMCF-MMF-SMF-FBG structure interferometer. The proposed structure is abbreviated as E7CFIs. The response of the device is highly sensitive to temperature and in-sensitive to RI. FBG is inscribed at the SMF lead-out section to cross-check the real-time temperature sensitivity of the E7CFIs. The wet etching of MCF is performed independently by using HF concentrated solution. The interferometer spectrum is enclosed MZI interference, which is caused by the central core light intensity coupled with the side cores that can be detected at the output of the proposed E7CFI. The transmission spectrum characteristics are controlled by the length of the MMF section. When the environment temperature changes, the transmission spectrum will be produced red-shift. On the other hand, a negligible blue-shift can be observed when performing RI sensing. Subsequently, the interferometer showed low RI sensitivity. Due to its compact structural design, the proposed E7CFIs exhibits ideal stability and repeatability during the experimental inspection.

The experimental setup includes the fabrication of the interferometer, the independent etching procedure, the working principle of the interferometer and the experimental demonstration are discussed in Section 2. Based on the theoretical analysis the simulations and experimental results are demonstrated in Section 3.

II. Experimental Setup

A. Fabrication of Interferometer

The schematic interferometer structure of the proposed E7CFIs is shown in Fig. 1. During the fabrication, the ordinary commercial step-index multimode fibers (MMFs) and MCF

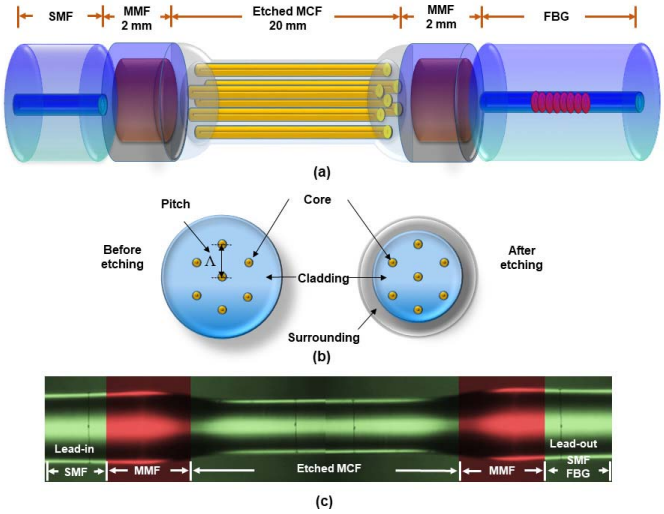

Fig. 1. (a) Schematic diagram of the E7CFI structure; (b) cross-section of MCF before and after etching; (c) E7CFI structure under microscope.

were used. The MMF length of each segment was about 2mm with the core and cladding diameters were 105μm and 125μm, respectively. The core and cladding diameters of MCF (FIBERCORE-SM-7C1500) were 6.1μm and 125μm, respectively. The MCF core pitch Λ between adjacent cores was 35μm. Further, three different EMCF segments having diameters of 84.7μm, 93.10μm, and 108.67μm were fabricated by etching, respectively. The length of each segment was 20 mm. The splicing segment of MMF and EMCF has produced a taper-like structure, as shown in Fig. 1(c). The design of the interferometer could be made unique because of its splicing and assembling was performed by independent etching of MCF. Further, it was assumed that the EMCF cross-section was weakly coupled and its side cores were uniformly distributed in the hexagonal transformation, as shown in Figure 1 (b). Then, the Taper-shaped MMF-EMCF-MMF segment was sandwiched between the SMF lead-in and lead-out, respectively. Finally, after finalizing the above-mentioned steps, three different E7CFIs were made, which were $\sim$ 84.7 μm, 93.10 μm, and 108.67 μm, respectively. In addition, the lead-out side of SMF was inscribed by an FBG at the wavelength of 1550 nm. The MMF section can be used to excite multiple modes and provide MZ interference so that all the cores carried by EMCF will be induced coupling.

B. Etching Setup and Monitoring

The MCF etching was performed independently. The schematic structure of the etching platform is shown in Fig. 2(a). The 10cm length of MCF was placed in the highly chemical-resistant test tube made up of PFA (perfluoroalkoxy: fluoroplastic) material. The purpose of longer length of MCF is to make 3-4 samples in one go. Secondly, we know that the etching rate of MCF Ge-doped silica cores are faster than the pure silica cladding. Consequently, the immersed end face of MCF in HF solution become waste, which was about 150$\sim$200μm. While fabrication of sensor, firstly cleaved the waste portion of MCF and then retained the remaining etched MCF to make 3-4 samples for sensor. The test tube

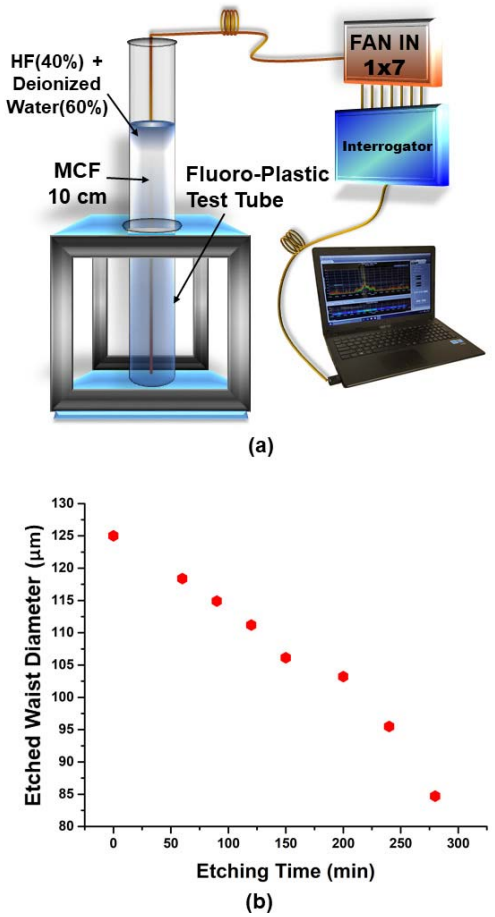

Fig. 2. Schematic diagram of (a) etching platform for MCF and (b) etching performance rate.

was filled with a concentrated solution. The concentrated solution consists of 40% HF and 60% deionized water and was used to perform the MCF etching. We deployed FAN-IN (manufactured by FIBERCORE) with an interrogator to synchronize data with the laptop so that the reflection spectrum can be monitored while etching. At the same time, we were gradually recorded different waist diameters of MCF, as shown in Fig. 2(b). The etching method [22] was followed during the etching process and the rate of change in waist diameter can be estimated as,

$$\mathrm{D}(t) = \mathrm{D}(t=0).\left[\frac{\mathrm{C}_{HF}(t)}{\mathrm{C}_{HF}(t=0}\right] \tag{1}$$

where, D(t) is the waist diameter, and $\mathrm{C}_{HF}(t)$ is the HF concentration. Fig. 2(b) depicts the nonlinearity, which was observed during the etching process. A non-linear trend appears in the output graph, which is due to the higher evaporation rate of HF in the surrounding medium than the deionized water. The slower etching rate can greatly help to achieve the desired smooth MCF waist diameter. As a result, slower etching techniques exhibit better control over the final waist diameter of the optical fibers. The finishing cross-section of the EMCF used for the experimental demonstration can be seen in Fig. 4(d-e). The microscopic images of fiber were recorded with a KEYENCE Digital microscope, VHX-100 series.

C. Working Coupling Principle

The coupling principle of an arbitrary dielectric coupled systems can be explained relative to the coupled-mode theory. The single-mode waveguides with linear interaction of N arbitrary mode and their propagation can be expressed as [36],

$$i\frac{d\mathrm{A}}{dz} = \overline{\mathrm{C_M}}\mathrm{A} \tag{2}$$

where, A is a vector element including the complex amplitude of the electric field of each core along the z-direction, and $\overline{C_{\mathrm{M}}}$ is regarded as a coupling matrix. Generally, $\overline{C_{\mathrm{M}}}$ explains the coupling interaction between a pair of the cores, and the coupling matrix $\mathrm{C_M}$ can be expressed as,

$$\overline{\mathrm{C_M}} = \begin{bmatrix} k_0 & c_{01} & c_{02} & \cdots & c_{0(N-1)} \\ c_{10} & k_1 & c_{12} & \cdots & c_{1(N-1)} \\ c_{20} & c_{21} & k_2 & \cdots & c_{2(N-1)} \\ \vdots & \vdots & \vdots & \ddots & \vdots \\ c_{(N-1)0} & c_{(N-1)1} & c_{(N-1)2} & \cdots & k_{(N-1)} \end{bmatrix} \tag{3}$$

where, k_i is the propagation constant of the fundamental mode of the i^{-th} waveguide, and c_{ij} is the coupling coefficient between the i^{-th} and j^{-th} cores. Generally, for independent waveguides, modes with different propagation constants are $k_i \neq k_j$, and these modes interact with each other under the condition of $c_{ij} \neq 0$. The $\overline{C_{\mathrm{M}}}$ coupling matrix can explain the interaction between waveguides in the form of the core pair. Ultimately, an arbitrary coupling technique can help to solve the matrix elements. Considering the weakly guided approximation, it can be explained the couplings between two parallel single-mode waveguides, and the coupling coefficient c of two identical cores with a circular geometry can be expressed as [37], [38],

$$c = \frac{\sqrt{2\Delta}}{r}\frac{u^2}{v^3}\left[\frac{K_0(w\delta_{ij}/r)}{(K_1(w))^2}\right] \tag{4}$$

where, r is the radius of MCF core, Δ is the relative refractive index difference between core and cladding, δ_{ij} is the distance between the $i^{-\mathrm{th}}$ core and $j^{-\mathrm{th}}$ core, and K_0 and K_1 are the modified Hankel functions of order 0 and 1, respectively. v is the normalized frequency equal to $(u^2 + w^2)^{1/2}$, u and w represent the normalized transverse propagation constants of the LP_{01} mode propagating in the core and cladding, respectively.

D. Experimental Demonstration

The experimental setup for temperature sensing is shown in Fig. 3. The fusion points of the interferometer are all spliced by a commercial splicer machine (COMCORE), using the manual MULTI MODE function in the fusion splicer menu. The spliced joint of MMF and EMCF has produced a taper-like structure, as shown in Fig. 4(a-c). The fiber cross-sections (assuming in xy-plane) with and without etched MCF can be seen in Fig. 4(d-f). Generally, when the light is launched in the E7CFIs from the SMF Lead-in to the MMF, the SMF core mode is coupled to the MMF core modes due to the greater modal mismatch between the SMF and the MMF, which is caused by multiple guided excitation modes. The MMF section

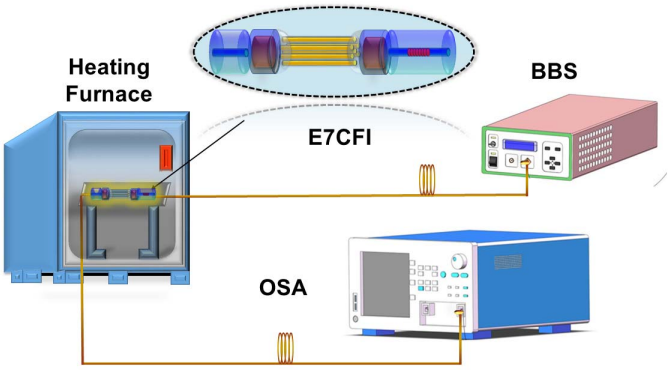

Fig. 3. Schematic experimental setup for measuring temperature.

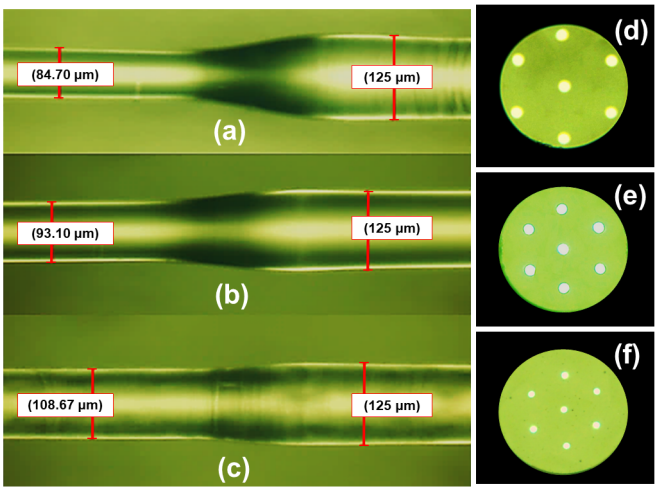

Fig. 4. Microscopic images for the E7CFIs, including a spliced section of MMF-EMCF by varying etched waist diameters along the z-direction (a) 84.70μm, (b) 93.10μm, (c) 108.67μm, and *xy*- cross section with etched MCF (d) 84.70μm, (e) 108.67μm, and without etched MCF (f) 125μm.

is implemented as a coupler to emit the coupled light from the central core to the six side cores, and then re-couple the light at the MMF to the SMF lead-out. At the SMF lead-out side, the inscribed FBG is performed like an interferometer's real-time cross-examiner while sensing, simultaneously. In the first MMF-EMCF section, the coupling phenomenon interacts, the transverse optical field is distributed at each core of the EMCF, and partially part of the energy is also coupled to the cladding mode. Similarly, the core modes and low-order cladding mode are recoupled and become part of the interference spectrum in the second section of EMCF-MMF. The derived transmission spectrum at each temperature set-point are recorded by an optical spectrum analyzer (OSA, YOKOGAWA AQ6370D), and the shift of these resonant dips are monitored with the change of external physical quantities in real-time. The transmission spectra with the different waists of the E7CFIs are shown in Fig. 5.

III. Result and Discussions

A. Simulations

COMSOL multi-physics® is employed to perform the simulations for the proposed E7CFIs. The finite element method (FEM) is used to simulate the modal field distribution of E7CFIs. These E7CFIs have different etched waist diameters

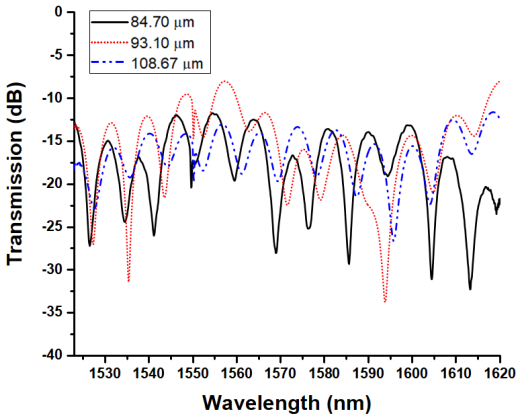

Fig. 5. Transmission spectrum of the E7CFIs by varying etched waist diameters at room temperature.

of 84.70μm, 93.10μm, and 108.67μm, respectively. It is assumed that the effective refractive index of each core of the MCF is 1.46, and the refractive index difference between the core and the cladding is taken as ~0.007. The original core-to-core pitch Λ of the MCF is 35μm with the core and cladding diameters are 6.1μm and 125μm, respectively. The core and cladding diameters of the MMFs section are 105μm and 125μm, and their refractive indices are 1.444 and 1.439, respectively. Both the core and cladding diameters of the SMF lead-in and lead-out are 9μm and 125μm, and their refractive indices are 1.462 and 1.457, respectively. The simulation parameters are consistent with utilized fibers for E7CFIs. When light is launched in the central core of the E7CFI, the transverse modal field distribution and normalized electric field mode are influenced by the side cores relative to the reduced waist diameter of the E7CFI. When light is launched into the EMCF through a segment of MMF, firstly several fundamental super-modes are excited at the first section of the MMF. Among them, some super-modes are degenerated in intensity with different phases across the core. Due to circular symmetry of fiber cores, only two super-modes are excited by the fundamental mode of SMF in the central core. When the excited super-modes propagate along the length of the EMCF segment, the interference between the two excited super-modes causes the continuous variation in the spatial patterns and can be recoupled from MMF back to the SMF lead-out. The energy field distribution of the two fundamental super-modes at $\lambda = 1550$ nm for three different waists of MCF are illustrated in Fig. 6(a-f).

On the other hand, the light field propagation and intensity distribution of the MMF-EMCF-MMF is simulated by using beam propagation method (BPM). In the simulation, the length of EMCF and MMF are maintained 20mm and 2mm, respectively. However, the etched cladding waist is varied from 84.7μm to original waist of MCF, as shown in Fig. 7(a-d). It can be seen from Fig. 7(a-d), the light is not only distributed in the center core but also distributed in hexagonal distributed cores of the MCF. It is more obvious, when the light is launched into the MMF then EMCF, the light is coupled and different modes are excited. In the excited modes only two fundamental super-modes could propagate. Here, the MMFs are used as a coupler, the two super-modes can be recoupled

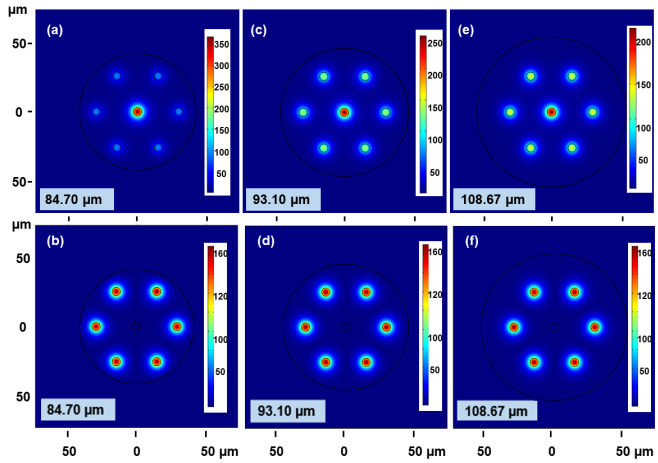

Fig. 6. COMSOL simulation result, two fundamental super-modes by varying etched waist (a), (b) 84.70μm, (c), (d) 93.10μm, and (e), (f) 108.67μm.

back at the second MMF and further become the part of MZ interference. The output value of central core is varied with the variation of etched waist of MCF, which is dominant and can be seen at output monitor value (a.u) of simulation result. The total output intensity of light can be expressed as,

$$I_{total} = I_1 + I_2 + 2\sqrt{I_1 I_2}\cos(\Delta\phi) \tag{5}$$

$\Delta\varphi$ is the phase difference between the two super-modes carried by I_1 and I_2, respectively. Here, $\Delta\varphi$ is the phase difference between two super-modes equal to $(2\pi\,\Delta n_{eff} L / \lambda)$, L is the length of EMCF, Δn_{eff} is the effective refractive index and λ is the operating wavelength. The MZI interference is formed due to the effective refractive index difference between the super-modes. The phase difference $\Delta\varphi$ between super-modes should be equal to $(2m+1)\pi$. Therefore, the attenuation peak can be determined as [28],

$$\lambda_m = \frac{2\Delta n_{eff} L}{2m+1} \tag{6}$$

Here, λ_m is the resonant wavelength and is directly related to L. According to (Eq. 6), the free spectral range (FSR) can be obtained as [29],

$$FSR = \Delta\lambda_m = |\lambda_m - \lambda_{m-1}| \approx \frac{\lambda_m^2}{\Delta n_{eff} L} \tag{7}$$

It can be clearly seen from Fig. 7(a-d), by reducing the waist diameters of the E7CFIs, the output power of the central core is different for different waists. This can be explained by the interaction between the central and side cores of the E7CFIs, which is caused by the thermo-optic coupling effect. When the environment temperature changes, the refractive index of the central core and the side core of the EMCF also varies. Due to the higher Germanium doping, the central core has a higher thermos-optic coefficient than the side cores. As shown in Fig.8(a), the simulation results showed that the central core energy distribution is significantly varied with the reduction of cladding waist of MCF. As a result, the refractive index difference between the central core and the side core becomes larger as the temperature increases. As shown in Fig. 8(b), simulated E7CFIs interference spectra

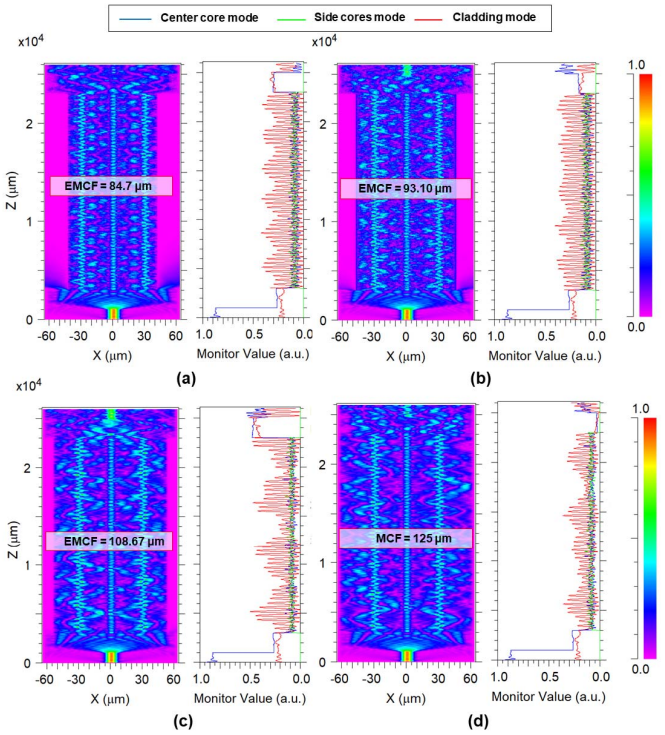

Fig. 7. Beam propagation of E7CFIs, with etched MCF (a) 84.70μm, (b) 93.10μm, (c) 108.67μm, and (d) without etched MCF ~125μm.

from 1520 nm to 1620 nm for different waists of EMCF are obtained. The variation in the coupling coefficient c is resulting FSR to be shifted.

B. Experiment and Transmission Characteristic Analysis

In order to illustrate the relationship between interference and the coupling principle, we selected three different waist diameters of the E7CFIs for the experiment. Fig. 5 shows the transmission spectra of E7CFIs with three different waist diameters of 84.70μm, 93.10μm, and 108.67μm at room temperature. The monitored light in the wavelength range of the optical spectrum analyzer (OSA) and the broadband light source (BBS) is 1520nm to 1620nm with a wavelength resolution of 0.02nm. The length of the EMCF and MMF determines the distribution of the transverse electric field in addition to the strength of coupling effect between the core modes. As per theoretical consent, the length of MMF~2 mm and EMCF~20mm is selected to obtain the desired transmission spectra. While investigating the temperature response of E7CFIs, the following expression can explain the relationship between temperature and interference wavelength [33],

$$\frac{d\lambda}{dT} = \frac{\lambda}{\Delta n_{eff}^{c,s}}\left[\frac{dn_{eff}^{c}}{dT} - \frac{dn_{eff}^{s}}{dT}\right] \tag{8}$$

where, T is the degree of temperature, λ is the dip wavelength of interference spectrum, n_{eff}^{c} and n_{eff}^{s} is the effective refractive indices of the central and side core modes, these two modes are called supper mode. $\Delta n_{eff}^{c,s}$ is the difference between the two effective refractive indices of super modes. However, the effective refractive index should be different between the central core mode and the side core mode.

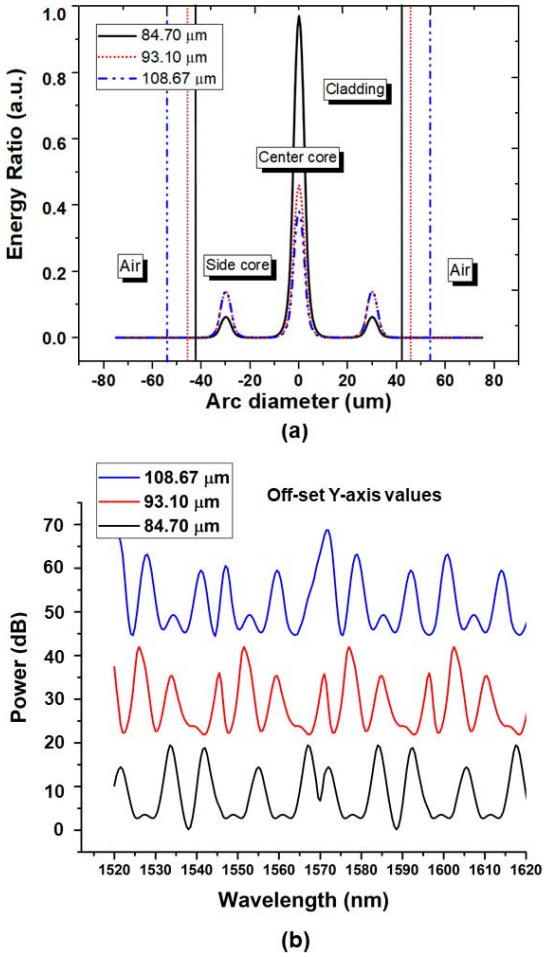

Fig. 8. Simulation result of E7CFIs (a) Comparing EMCF, central core energy distribution, (b) Interference spectrum.

According to Eq. (8), the following conditions must be satisfied to realize the relationship between λ and T.

$$\left[\frac{dn^{c}_{eff}}{d\mathrm{T}} - \frac{dn^{s}_{eff}}{d\mathrm{T}}\right] \neq 0 \tag{9}$$

The λ and T describe the dip wavelength of the interference spectrum. Where, λ can shift as the temperature increases or decreases. In the experimental setup, the temperature is measured with a 10°C shift from 24°C to 130°C. Fig. 9(a-c) describes the transmission spectral response of different E7CFIs. As the temperature increases or decreases, the spectrum has produced red-shift or blue-shift, respectively. The linear relationship between the temperature and the interference dip is traced by observing red-shift, as shown in Fig. 10(a). The E7CFIs exhibits the sensitivity of 103.2pm/°C within the ambient temperature up-to 70°C. In addition, for different E7CFI waists of 84.70μm, 93.10μm, 108.67μm, the sensitivity is 89.19pm/°C, 66.64pm/°C, 56.42pm/°C in the range of 24°C to 130°C, and linearity is 0.991, 0.998, 0.997, respectively. The average sensitivity of the inscribed FBG is 13pm/°C, which is consistent with the conventional FBG [39], as shown in Fig. 10(b). Here, FBG is implemented as a real-time cross checker for E7CFIs. According to the analysis performed through experimental demonstration, the proposed

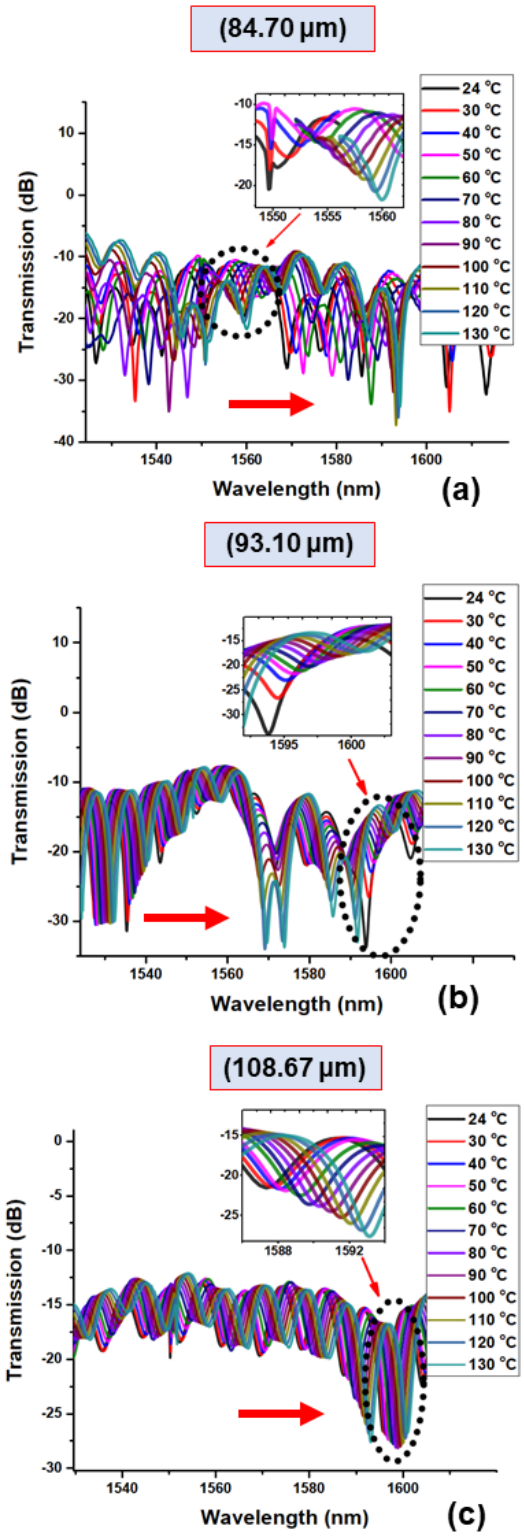

Fig. 9. Spectral response to temperature for E7CFIs by varying cladding waist (a) 84.70μm, (b) 93.10μm, and (c) 108.67μm.

E7CFIs are significantly improved the temperature sensitivity, which is 8 times better than that of the conventional FBGs.

Moreover, as shown in Fig. 11(a-d), the RI responses of the interferometers are also experimentally investigated. According to RI responses of the different waists of E7CFIs, the interferometers are produced a slight blue-shift in the range of 1.34 and 1.38. The E7CFIs with waist diameters

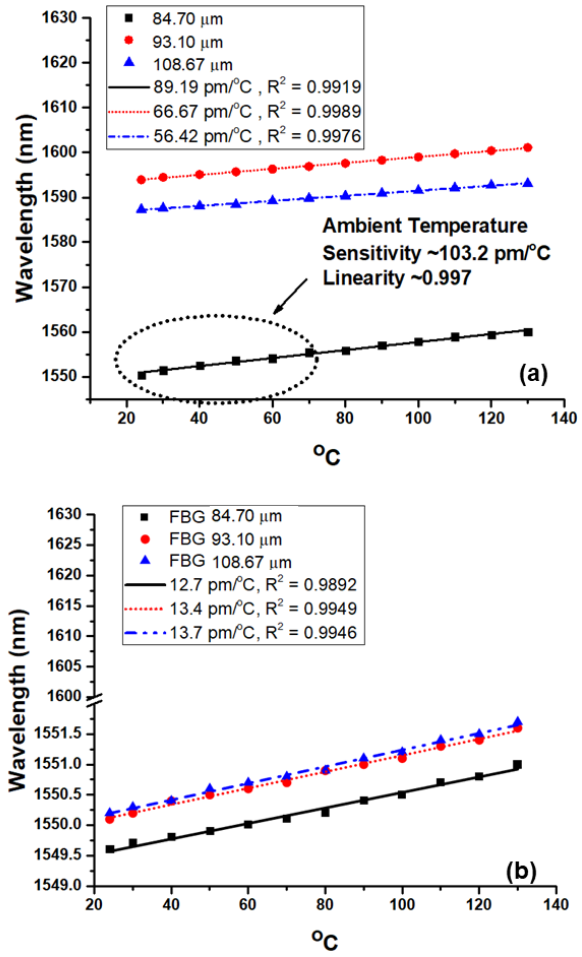

Fig. 10. Sensitivity and linearity response of three different waist diameters of 84.70μm, 93.10μm, 108.67μm, (a) E7CFIs (b) Inscribed FBG response.

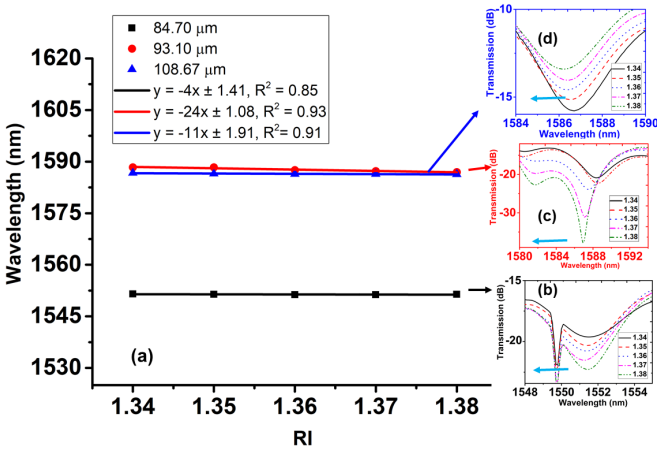

Fig. 11. Surrounding Refractive index (a) linearity and sensitivity response by varying etched waist diameter of E7CFIs (b) 84.70 μm, (c) 93.10 μm, (d) 108.67 μm.

of 84.70μm, 93.10μm, 108.67μm have displayed the RI sensitivity of −4nm/RIU, −24nm/RIU, −11nm/RIU, with the linearity of 0.85, 0.93, and 0.91, respectively. The RI-insensitive response is instigated by the surrounding RI. As the surrounding RI becomes larger, the effective refractive index of the MCF cladding mode can be produced a slight blue-shift in wavelength. This is caused by the coupling phenomenon between the central and the side cores of MCF. As we know that the EMCF pitch Λ between all cores is constant during etching. There are two different techniques that can produce a stronger evanescent field to maintain RI sensitivity; one is to reduce the pitch Λ distance between the central and the side cores by tapering or else, and the other is to maintain the extended length of MCF. In the proposed E7CFI design, a shorter length of EMCF is chosen, which is not sufficient to expose the stronger evanescent field in the surrounding medium. Consequently, the refractive index of the core mode to the surrounding medium becomes much smaller. As a result, the E7CFIs wavelength shifted very slightly, as shown in Fig. 11(b-d). The experimental results demonstrate that when the cladding waist is etched near to the hexagonal distributed outer cores, the RI insensitivity increased. Hence, the RI response of E7CFIs is as low as insensitive. This is an advantageous feature of the proposed E7CFIs, which showed a good response on one parameter and can be suppressed other parameter. In addition, E7CFIs are also provided excellent compatibility, repeatability, and stability during experimental demonstrations.

IV. Conclusion

In conclusion, an interferometer based on MZI etched multi-core coupled structure is proposed. Its novel advantageous feature includes insensitive to RI and highly sensitive to temperature. The E7CFIs structure is fabricated by an independent slow etching methodology. The tuning of the interferometer is controlled by an appropriate etching technique. The experimental results showed that E7CFIs not only a temperature sensitive having sensitivity as high as 103.2pm/°C in the ambient temperature up to 70°C, but is also RI insensitive, so it can be easily distinguished similar MZI sensors that have been reported, with a sensitivity of only 54.57pm/°C [3], 72.17pm/°C [35] and FBGs [39]. In the demonstration, compared with the conventional FBG, the responsiveness and sensitivity of the E7CFI is improved by 8 times. In contrast, based on the best experimental and simulation results, it is suggested that the proposed E7CFIs structure can also be used as a potential candidate for the measurement of higher temperature sensing up to 1000°C. The proposed E7CFIs may find the possibility of using this sensing architecture in a wide range of practical applications, such as optics, environmental sciences, life sciences, chemistry, medicine, and communication models.

Disclosures: *No potential conflict of interest was reported by the authors.*

References

[1] C. G. Askins, G. A. Miller, and E. J. Friebele, "Bend and twist sensing in a multi-core optical fiber," in *Proc. 21st Annu. Meeting IEEE Lasers Electro-Opt. Soc. (LEOS)*, Nov. 2008, pp. 109–110.

[2] S. F. S. M. Noor, S. W. Harun, H. Ahmad, and A. R. Muhammad, "Multimode interference based fiber-optic sensor for temperature measurement," in *Proc. J. Phys., Conf. Ser.*, Mar. 2019, vol. 1151, no. 1, Art. no. 012023.

[3] S. Duan *et al.*, "Intensity-interrogated refractive index sensor based on exposed-core multicore fiber mach-Zehnder interferometer," in *Proc. CLEO: Sci. Innov.*, May 2019, pp. 1–2, Paper SF3L.7.

[4] Y. Liu, A. Zhou, and L. Yuan, "Gelatin-coated michelson interferometric humidity sensor based on a multicore fiber with helical structure," *J. Lightw. Technol.*, vol. 37, no. 10, pp. 2452–2457, May 15, 2019.

[5] I. Floris, S. Sales, P. A. Calderón, and J. M. Adam, "Measurement uncertainty of multicore optical fiber sensors used to sense curvature and bending direction," *Measurement*, vol. 132, pp. 35–46, Jan. 2019.

[6] J. Li, Q. He, Z. Chen, and X. Fang, "Simultaneous measurement of three parameters based on an up-tapered fiber cascaded with a droplet-like multimode interferometer," *OSA Continuum*, vol. 2, no. 4, pp. 1113–1124, Mar. 2019.

[7] S. Pevec and D. Donlagic, "MultiParameter fiber-optic sensor for simultaneous measurement of thermal conductivity, pressure, refractive index, and temperature," *IEEE Photon. J.*, vol. 9, no. 1, pp. 1–14, Feb. 2017.

[8] Y. Awaji, T. Kobayashi, and T. Takahata, "Multicore/multimode fiber coupling device," U.S. Patent 15 306 104, Feb. 16, 2017.

[9] Y. Zhao, L. Cai, and H.-F. Hu, "Fiber-optic refractive index sensor based on multi-tapered SMS fiber structure," *IEEE Sensors J.*, vol. 15, no. 11, pp. 6348–6353, Nov. 2015.

[10] A. Sun, Z. Wu, D. Fang, J. Zhang, and W. Wang, "Multimode interference-based fiber-optic ultrasonic sensor for non-contact displacement measurement," *IEEE Sensors J.*, vol. 16, no. 14, pp. 5632–5635, May 2016.

[11] J. W. Costa, M. A. R. Franco, V. A. Serrão, C. M. B. Cordeiro, and M. T. R. Giraldi, "Macrobending SMS fiber-optic anemometer and flow sensor," *Opt. Fiber Technol.*, vol. 52, Nov. 2019, Art. no. 101981.

[12] L. Hou, X. Zhang, J. Yang, J. Kang, and L. Ran, "Simultaneous measurement of refractive index and temperature based on half-tapered SMS fiber structure with fringe-visibility difference demodulation method," *Opt. Commun.*, vol. 433, pp. 252–255, Feb. 2019.

[13] Y. Sun *et al.*, "High sensitivity optical fiber strain sensor using twisted multimode fiber based on SMS structure," *Opt. Commun.*, vol. 405, pp. 416–420, Dec. 2017.

[14] Y. Cardona-Maya, I. Del Villar, A. B. Socorro, J. M. Corres, I. R. Matias, and J. F. Botero-Cadavid, "Wavelength and phase detection based SMS fiber sensors optimized with etching and nanodeposition," *J. Lightw. Technol.*, vol. 35, no. 17, pp. 3743–3749, Sep. 1, 2017.

[15] C. Zhang, T. Ning, J. Li, L. Pei, C. Li, and H. Lin, "Refractive index sensor based on tapered multicore fiber," *Opt. Fiber Technol.*, vol. 33, pp. 71–76, Jan. 2017.

[16] Y.-F. Qi *et al.*, "Research on refractive index sensor based on multi-core micro-nano fiber," in *Proc. Asia Commun. Photon. Conf. (ACP)*, Oct. 2018, pp. 1–3.

[17] Y. Chunxia, D. Hui, D. Wei, and X. Chaowei, "Weakly-coupled multicore optical fiber taper-based high-temperature sensor," *Sens. Actuators A, Phys.*, vol. 280, pp. 139–144, Sep. 2018.

[18] Y. Jiang *et al.*, "Simultaneous measurement of refractive index and temperature with high sensitivity based on a multipath fiber Mach–Zehnder interferometer," *Appl. Opt.*, vol. 58, no. 15, pp. 4085–4090, May 2019.

[19] H. Yu, D. Guo, L. Wu, C. Li, and W. Hu, "RI sensitivity of tapered MCF enhanced by graphene coating," in *Proc. Conf. Lasers Electro-Opt.*, 2019, pp. 1–2, Paper JTh2A.59.

[20] P. Xian, G. Feng, Y. Ju, W. Zhang, and S. Zhou, "Single-mode all-fiber structured modal interference for temperature and refractive index sensing," *Laser Phys. Lett.*, vol. 14, no. 8, Jul. 2017, Art. no. 085101.

[21] X.-Y. Sun *et al.*, "Highly sensitive refractive index fiber inline Mach–Zehnder interferometer fabricated by femtosecond laser micromachining and chemical etching," *Opt. Laser Technol.*, vol. 77, pp. 11–15, Mar. 2016.

[22] E. J. Zhang, W. D. Sacher, and J. K. S. Poon, "Hydrofluoric acid flow etching of low-loss subwavelength-diameter biconical fiber tapers," *Opt. Express*, vol. 18, no. 21, pp. 22593–22598, Oct. 2010.

[23] M. T. Lee, "Reaction of high-silica optical fibers with hydrofluoric acid," *J. Amer. Ceram. Soc.*, vol. 67, no. 2, pp. C-21–C-22, Feb. 1984.

[24] Q. Yao *et al.*, "Simultaneous measurement of refractive index and temperature based on a core-offset Mach-Zehnder interferometer combined with a fiber Bragg grating," *Sens. Actuators A, Phys.*, vol. 209, pp. 73–77, Mar. 2014.

[25] L. Y. Fan, W. W. Jiang, R. F. Zhao, L. Pei, and S. S. Jian, "Temperature characteristic of in-fiber Mach–Zehnder interferometer using twin-core fiber," *Opt. Precis. Eng.*, vol. 1, pp. 1–5, Jan. 2011.

[26] L. Li, L. Xia, Z. Xie, L. Hao, B. Shuai, and D. Liu, "In-line fiber Mach-Zehnder interferometer for simultaneous measurement of refractive index and temperature based on thinned fiber," *Sens. Actuators A, Phys.*, vol. 180, pp. 19–24, Jun. 2012.

[27] F. Liu, H. F. Lin, Y. Liu, A. Zhou, and Y. T. Dai, "Femtosecond-induced spiral micro-structured SMS fiber structure for refractive index measurement," *Opt. Express*, vol. 26, no. 13, pp. 17388–17396, Jun. 2018.

[28] Q. Wang and Y. Liu, "Optical fiber curvature sensor based on MMF-SCF-MMF structure," *Opt. Fiber Technol.*, vol. 43, pp. 1–5, Jul. 2018.

[29] S. Zhou, B. Huang, and X. Shu, "A multi-core fiber based interferometer for high temperature sensing," *Meas. Sci. Technol.*, vol. 28, no. 4, Feb. 2017, Art. no. 045107.

[30] A. Van Newkirk, Z. S. Eznaveh, E. Antonio-Lopez, G. Salceda-Delgado, A. Schülzgen, and R. Amezcua-Correa, "High temperature sensor based on supermode interference in multicore fiber," in *Proc. Conf. Lasers Electro-Opt. (CLEO)-Laser Sci. Photon. Appl.*, Jun. 2014, pp. 1–2.

[31] J. E. Antonio-Lopez, Z. S. Eznaveh, P. LiKamWa, A. Schülzgen, and R. Amezcua-Correa, "Multicore fiber sensor for high-temperature applications up to 1000° C," *Opt. Lett.*, vol. 39, no. 15, pp. 4309–4312, Aug. 2014.

[32] L. Duan *et al.*, "Heterogeneous all-solid multicore fiber based multipath Michelson interferometer for high temperature sensing," *Opt. Express*, vol. 24, no. 18, pp. 20210–20218, Sep. 2016.

[33] X. Wang, D. Chen, H. Li, G. Feng, and J. Yang, "In-line Mach–Zehnder interferometric sensor based on a seven-core optical fiber," *IEEE Sensors J.*, vol. 17, no. 1, pp. 100–104, Jan. 2017.

[34] Q. Liu, S.-W. Wang, X.-H. Fu, G.-W. Fu, W. Jin, and W.-H. Bi, "Refractive index insensitive temperature sensor based on waist-enlarged few mode fiber bitapers," *Optoelectron. Lett.*, vol. 13, no. 1, pp. 25–28, Jan. 2017.

[35] X. Fu, H. Xie, X. Zeng, G. Fu, and W. Bi, "Refractive index insensitive temperature sensor based on specialty triple-clad fiber," *Opt. Express*, vol. 23, no. 3, pp. 2320–2327, Jan. 2015.

[36] N. Kishi and E. Yamashita, "A simple coupled-mode analysis method for multiple-core optical fiber and coupled dielectric waveguide structures," *IEEE Trans. Microw. Theory Techn.*, vol. 36, no. 12, pp. 1861–1868, Dec. 1988.

[37] Y. Murakami and S. Sudo, "Coupling characteristics measurements between curved waveguides using a two-core fiber coupler," *Appl. Opt.*, vol. 20, no. 3, pp. 417–422, Feb. 1981.

[38] A. W. Snyder, "Coupled-mode theory for optical fibers," *J. Opt. Soc. Amer.*, vol. 62, no. 11, pp. 1267–1277, Nov. 1972.

[39] Y.-J. Rao, "In-fibre Bragg grating sensors," *Meas. Sci. Technol.*, vol. 8, no. 4, pp. 355–375, 1997.